frontiers | Frontiers in Marine Science

TYPE Original Research
PUBLISHED 23 May 2024
DOI 10.3389/fmars.2024.1410241

OPEN ACCESS

EDITED BY
Selvaraj Kandasamy,
Central University of Tamil Nadu, India

REVIEWED BY
Xiting Liu,
Ocean University of China, China
Yuan-Pin Chang,
National Sun Yat-sen University, Taiwan
Huawei Wang,
Southern University of Science and Technology, China

*CORRESPONDENCE
Jianfeng Su
jfsu@tongji.edu.cn
Daidu Fan
ddfan@tongji.edu.cn

RECEIVED 31 March 2024
ACCEPTED 08 May 2024
PUBLISHED 23 May 2024

CITATION
Wang C, Su J, Song L, Qiao P and Fan D (2024) Response of early diagenesis to methane leakage in the inner shelf of the East China Sea.
Front. Mar. Sci. 11:1410241.
doi: 10.3389/fmars.2024.1410241

Response of early diagenesis to methane leakage in the inner shelf of the East China Sea

Chenpei Wang[1], Jianfeng Su[1,2]*, Lei Song[1], Peijun Qiao[1] and Daidu Fan[1,3]*

[1]State Key Laboratory of Marine Geology, Tongji University, Shanghai, China, [2]Zhoushan Field Scientific Observation and Research Station for Marine Geo-hazards, China Geological Survey, Zhoushan, China, [3]Laboratory for Marine Geology, Qingdao Marine Science and Technology Center, Qingdao, China

Shelf seas are experiencing a rise in shallow gas leaks, primarily methane, raising concerns due to their environmental impact. However, the effect of the leaks on early diagenesis remains poorly understood. This study analyzes sediment lithology, organic geochemistry and porewater geochemistry of two short cores collected nearby the pockmarks in the muddy inner shelf of the East China Sea. Our findings clearly demonstrate the impact of methane leakage on early diagenesis, evidenced by the shallower position of the SMTZ (sulfate-methane transition zone), higher concentrations of uranium (U), vanadium (V), and manganese (Mn) in the porewater near and above the SMTZ, and downcore decrease in Mg^{2+}, Ca^{2+}, and Sr^{2+} concentrations versus increase in Mg^{2+}/Ca^{2+} and Sr^{2+}/Ca^{2+} ratios. Their profile variations and the difference between two cores are determined by the intensity of methane leakage. The estimated methane diffusive flux of 619 mmol m^{-2} yr^{-1} at YEC7–2 is roughly 8.5 times that at YEC7–1 (73 mmol m^{-2} yr^{-1}), consistent with a shorter distance of YEC7–2 to the pockmark with active methane leakage. A schematic model is summarized to demonstrate the response of early diagenesis processes to the increasing methane leakages in response to changing sedimentation regimes from accretion to severe erosion. This study undoubtedly improves our understanding mutual promotion effect between seafloor erosion and gas leakage, and their impact on early diagenesis processes and resultant porewater geochemical changes and authigenic mineral records.

KEYWORDS

methane leakage, anaerobic oxidation of methane, porewater geochemistry, East China Sea, early diagenesis

1 Introduction

Methane (CH_4), a potent greenhouse gas, exerts a disproportionate influence on oceanic biogeochemistry and air-sea gas exchange, though methane emission from the ocean constitutes only 2% of its global flux (Reeburgh, 2007; Letcher, 2019). Large-scale seafloor releases of methane pose a significant environmental threat, potentially triggering

geological hazards (landslides, earthquakes) and exacerbating global warming, ocean acidification, and disruption of marine ecosystems (Chen et al., 2020). Therefore, to better understand the potential impacts of methane leakage on global climate change, it is crucial to identify methane seepage through a series of geochemical approaches.

Microbial activity is responsible for the majority (85%) of global annual methane production and a significant portion (60%) of its consumption (through anaerobic oxidation, AOM) (Knittel and Boetius, 2009; Sela-Adler et al., 2015). This, combined with the aerobic oxidation of methane in the water column, helps prevent methane escape into the atmosphere (Mao et al., 2022). In anoxic environments, the final step of organic matter breakdown via anaerobic digestion produces methane (Knittel and Boetius, 2009). As this methane migrates upwards, it encounters sulfate in the porewater, triggering AOM by microbial communities. This process utilizes sulfate as an electron acceptor, converting both methane and sulfate into bicarbonate and hydrogen sulfide, respectively (Equation 1; Boetius et al., 2000).

$$CH_4 + SO_4^{2-} \rightarrow HCO_3^- + HS^- + H_2O \quad (1)$$

AOM acts as a vital sink for methane in marine settings, consuming a substantial 90% of the gas via its reaction with dissolved sulfate in porewater profiles (Boetius and Wenzhöfer, 2013). This process functions as a key biogeochemical filter, effectively mitigating methane emissions to the atmosphere and contributing to the regulation of atmospheric greenhouse gas (GHG) concentrations (Haroon et al., 2013).

However, methane migration to the seafloor alters the redox state within sediments. AOM processes demonstrably influence the surface contents of redox-sensitive elements and the reconstruction of bottom water redox conditions (Schoepfer et al., 2015; Miao et al., 2022). It is widely recognized that due to AOM influence, sediments often exhibit uranium enrichment, high calcium content, and the presence of a "barium front" (Peketi et al., 2012; Peketi et al., 2015). Consequently, methane leakage significantly affects the distribution and behavior of these elements in the sediment column (Hu et al., 2015; Lin et al., 2022). Recent studies have highlighted the utility of sediment porewater geochemistry as a reliable indicator of past and present methane leakage events (Feng et al., 2018; Xu et al., 2018). By analyzing specific geochemical signatures within porewater profiles, researchers can reconstruct historical methane leakage activity (Hensen et al., 2003; Sivan et al., 2011). Therefore, detailed geochemical investigations of modern porewater compositions provide a valuable tool for elucidating the biogeochemical consequences of methane leakage.

Shelf seas exhibit a substantially higher methane flux compared to the open ocean (Bange et al., 1994; Rhee et al., 2009). Shelf seas are characterized by widespread occurrences of shallow gas, which is composed of 94.45% of CH_4, 3.78% of N_2, and 1.80% of CO_2 in the ECS (Chen et al., 2008), and typically the byproducts of organic matter biodegradation at relatively shallow burial depths (Fleischer et al., 2001; Judd and Hovland, 2007). Intensified human activities have concerningly reduced sediment input and exacerbated coastal erosion, thinning the cap layer of shallow gas and enhancing leakages (Yang et al., 2011; Deng et al., 2017). The ECS continental shelf is a key area for studying both shallow gas and methane-related anaerobic processes, as evidenced by recent researches (Xu et al., 2018; Liu et al., 2020a; Zhang et al., 2021). Chen et al. (2020) used high-resolution seismic exploration to map shallow gas distribution in the ECS's Holocene sediments, suggesting the thickness of Holocene mud wedge control the shallow gas distribution which is vulnerable to coastal erosion. Conversely, Liu et al. (2020b) investigated how sedimentation dynamics influence sulfate reduction on the ECS shelf, highlighting the role of sedimentation rate variations in controlling the movement of the sulfate-methane transition zone (SMTZ). However, our understanding of how seabed erosion-induced methane leakage impacts early diagenetic processes in the ECS remains limited and necessitates further investigation.

This study focuses on the potential for methane leakage in the ECS inner shelf, specifically near Dongji Island, Zhoushan Archipelago. This integrated analyses of sedimentology, porewater geochemistry, and organic geochemistry in two short cores will be used to unravel the impact of methane leakage on early diagenetic processes within these marine sediments. We will further explore the potential link between seabed erosion and these leakage events.

2 Regional setting

The Zhoushan sea area, situated on the northwestern ECS shelf (Figure 1), acts as a critical conduit for Yangtze River sediment delivery to the ECS. This region experiences the combined influence of nutrient-rich Yangtze River discharge and the intrusion of the Taiwan Warm Current (Jiao et al., 2007). Consequently, the ECS shelf boasts high primary productivity, ranging from 108 to 997 mg m^{-2} d^{-1} with an average of 425 mg m^{-2} d^{-1} (Gong et al., 2003). Furthermore, substantial terrestrial input, including organic carbon (OC), from rivers significantly contributes to sedimentary OC (Yang et al., 2013; Shi et al., 2015).

The Yangtze River Delta (YRD) and surrounding areas are characterized by widespread occurrences of shallow gas within the muddy sediments (Hu et al., 2016; Qiu et al., 2018). Typically buried within a few meters to tens of meters, with most deposits found at water depths less than 100 meters (Li et al., 2010), these shallow gas accumulations are particularly concentrated in Hangzhou Bay, as evidenced by acoustic blanking in seismic profiles (Song et al., 2023). This coincides with a shoreward increase in methane concentrations observed in ECS shelf waters (Ye et al., 2016; Sun et al., 2018). Moreover, the operation of the Three Gorges Dam (TGD) has significantly reduced suspended sediment discharge by approximately 70% (Guo et al., 2021). This has led to a shift in the Yangtze subaqueous delta, transitioning from rapid accretion to pronounced erosion, with the effects extending into Hangzhou Bay (Xie et al., 2013; Guo et al., 2021). The combination of gassy sediment and erosion significantly weakens the stability of seabed sediments, potentially inducing changes in seabed topography (Cathles et al., 2010).

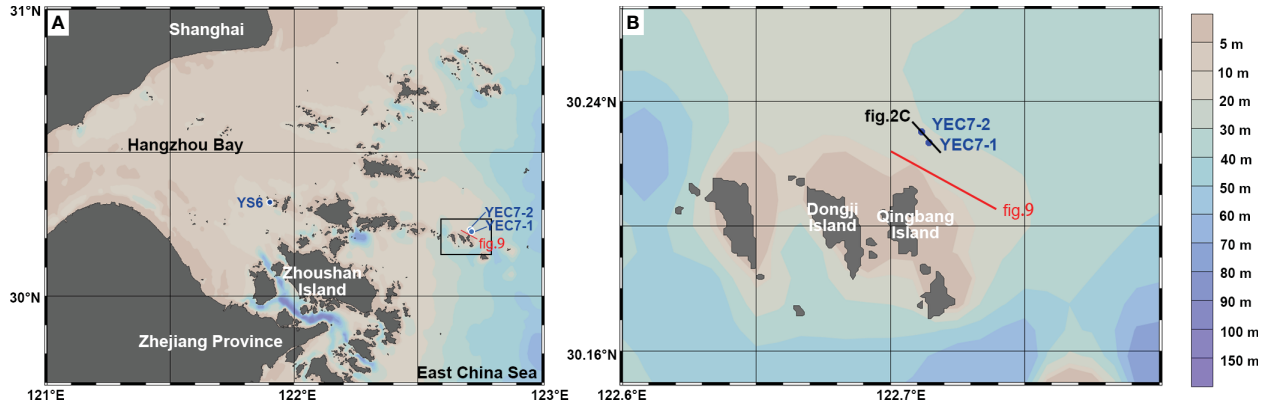

FIGURE 1
Geographical locations of the Hangzhou Bay and the Zhoushan Islands **(A)**, and the locations of short cores (YEC7–1 and YEC7–2, collected in 2022 for this study), the multibeam scanning profile and the sub-bottom profile in Hangzhou Bay and the ECS inner shelf **(B)**. Data of core YS6 is reproduced from He et al. (2020). The multibeam scanning profile across YEC7–1 and YEC7–2, marked in black line, is reinterpreted in Figure 2C. The sub-bottom profile, marked in red line, is reinterpreted in Figure 9 (Yang et al., 2021).

3 Materials and methods

3.1 Multibeam acoustic surveys and short core collections

A bathymetric survey conducted in July 2022 aboard the R/V "Zhe Yu Ke 2" in the northeastern waters near Dongji Island, Zhoushan Archipelago (Figure 1), identified a depression with potential gas release activity using a multibeam echosounder system (Teledyne Reson) within the targeted sampling area (Figure 2). Two gravity cores were collected: YEC7–2 from the center of the depression and YEC7–1 from a location outside the depression (Table 1). The two core locations are separated by a straight-line distance of approximately 373.5 m.

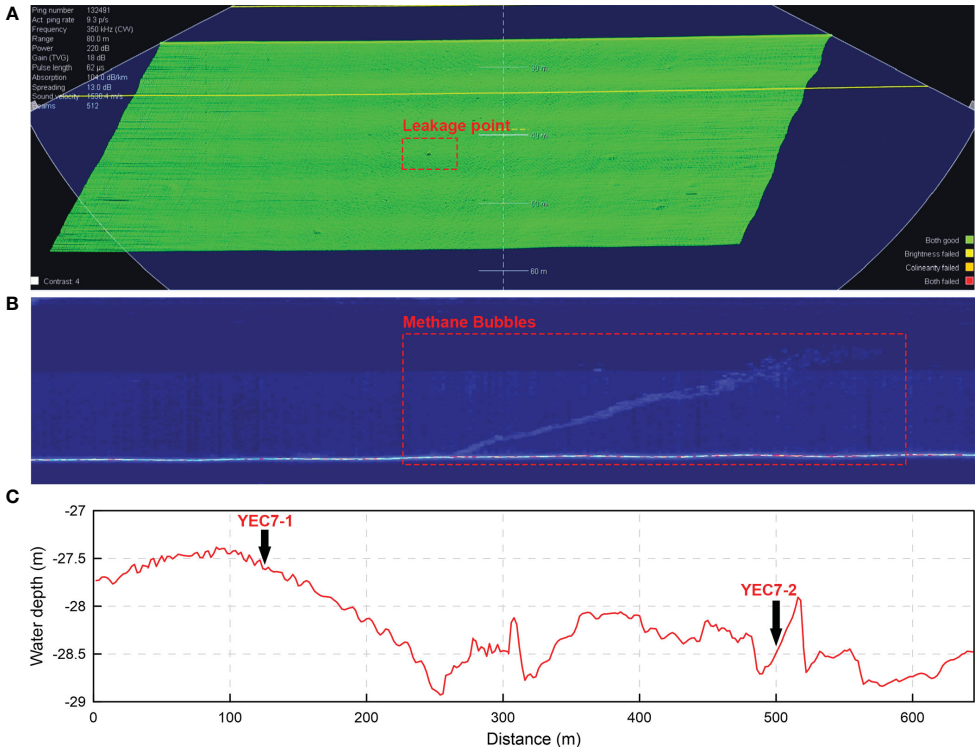

FIGURE 2
Multibeam scanning seafloor topography map of the study pockmark with an active leakage point during the survey **(A)**; active methane outflow from the gassy sediments in the multibeam snapshot **(B)**; the multibeam scanning profile across YEC7–1 and YEC7–2 **(C)**.

TABLE 1 Location and methane seepage information of two short cores.

Core	Longitude	Latitude	Water depth	Core length	Methane seepage
YEC7–1	122°42.851′ E	30°13.613′ N	27.7 m	3.05 m	Low impact
YEC7–2	122°42.691′ E	30°13.815′ N	28.4 m	2.25 m	High impact

3.2 Porewater and methane samples collections

Upon core retrieval, porewater samples (at 2–20 cm intervals) and sediment samples for methane analysis (at 10–30 cm intervals) were collected immediately onboard. Porewater (around 20 mL) were extracted from each layer using negative pressure and dispensed equally into 10 mL LDPE bottles pre-designated for anion and cation analyses, respectively. For cation analysis, subsamples were acidified with 20 μL of ultrapure hydrochloric acid. All bottles were then sealed securely and stored at 4°C.

Sediment samples for methane analysis (20 mL) were taken using a syringe without the head, and immediately transferred into 50 mL headspace vials, which contained 15 mL of 1 mol L^{-1} NaOH solution to inhibit methane-producing bacteria activity. Then, the bottle was purged with nitrogen for 1 minute, sealed with a rubber stopper and an aluminum cap, shaken, and stored at the container of 4°C.

3.3 Laboratory analyses

In total, 46 porewater samples from two short cores were analyzed for concentrations of major elements (Mg), trace elements (Ca, V, Mn, Sr, Ba, U), and anions (SO_4^{2-}, Cl^-). Methane concentration and carbon and hydrogen isotopes were determined for methane samples. Sediment grain size, OC content and carbon isotopic compositions, activities of total ^{210}Pb, were also measured.

3.3.1 Sediment OC geochemical, grain size and sedimentation rate analyses

Approximately 1 g of dry sediment sample was weighed into a centrifuge tube and acidified with 15 mL of 1 mol/L HCl solution. The mixture was thoroughly mixed, shaken in a 60°C water bath for 3 hours, and then centrifuged for 5 minutes after standing for 18 hours. The supernatant was discarded, and the sample was repeatedly washed with deionized water (3–4 times) until the pH of the rinseate reached near neutral (pH ≈ 7). The sample was then oven-dried at 40°C. Subsequently, around 10 mg of the ground sample powder was wrapped in tin foil for analysis. Total organic carbon (OC) content and its isotopic composition ($\delta^{13}C$) were determined using an elemental analyzer (Thermo-Flash EA) coupled with a gas chromatography-isotope ratio mass spectrometer (GC-IRMS, Thermo Scientific) at the State Key Laboratory of Marine Geology, Tongji University.

Approximately 0.3 g of dry sediment sample was weighed into a container and treated with 15 mL of 30% hydrogen peroxide (H_2O_2) solution. The mixture was heated in a 60°C water bath at a constant temperature for 4 hours until gas evolution ceased. The suspension was then centrifuged for 5 minutes, and the supernatant was discarded. To remove carbonate minerals, 15 mL of 1 mol/L hydrochloric acid (HCl) was added to the residue (Fan et al., 2015). The mixture was again heated in a 60°C water bath for 4 hours until gas evolution stopped. After centrifugation (5 minutes), the supernatant was discarded. This acidification step was repeated three times to ensure complete carbonate removal. Sediment grain size distribution was subsequently measured using a BECKMAN LS-230 laser particle size analyzer at the State Key Laboratory of Marine Geology, Tongji University.

Samples for sedimentation rate analysis were selected at intervals of 4–10 cm from both cores. Approximately 8 g of dry sediments were sealed for each sample and sat for at least 20 days to allow for radon ingrowth. Gamma-ray measurements were conducted using an HPGe well-type γ-ray detector (GWL-120–15-LB-AWT, AMETEK) with a counting efficiency higher than 50% and an energy resolution of 2.3 keV (at 1332 keV). Gamma spectrometry provided results for supported ^{210}Pb (via daughters ^{214}Pb and ^{214}Bi based on photo peaks at 295.0 and 351.9 keV), total ^{210}Pb (at 46.5 keV), and ^{137}Cs (at 661.6 keV). Excess ^{210}Pb (^{210}Pbex) activity was determined by subtracting the supported from total ^{210}Pb. All ^{137}Cs activities were below the minimum detectable activity. Therefore, sedimentation rate analysis was based on ^{210}Pbex results.

3.3.2 Porewater samples analyses

Porewater samples were tested by diluting 1000 times in order to accurately measure the concentration of sulfate. Testing was conducted using the Waters e2695 Alliance high-performance liquid chromatography system from Waters Corporation at the State Key Laboratory of Marine Geology, Tongji University.

The concentrations of major elements were determined using the inductively coupled plasma optical emission spectrometer (ICP-OES IRIS Advantage) with an analysis precision of less than 0.5%. The concentrations of trace elements were determined using the inductively coupled plasma mass spectrometer (ICPMS) with model Agilent 7900 at the State Key Laboratory of Marine Geology, Tongji University.

3.3.3 Methane samples analyses

Methane concentrations were determined in headspace gas samples collected from the same or adjacent sediment core intervals as the porewater samples. Anaerobic sample bottles containing sediment were vigorously shaken to promote equilibration of methane between the gas and liquid phases. Analyses were performed using an Ultra Trace gas chromatograph (GC-TCD) and a MAT253 isotope ratio mass spectrometer (GC-C/IRMS) from Shimadzu Corporation at the Qingdao Institute of Marine Geology, China Geological Survey. The instruments achieved a precision of less than 3% and a detection limit of 1 ppm for CH_4.

3.4 Estimation of Sulfate-methane interface depth and methane diffusive flux

Sulfate concentrations were fitted using the least squares linear regression method, and the fitted line was extrapolated to a sulfate concentration of zero to accurately determine the depth of SMI (Yang et al., 2010; Hu et al., 2015). It was assumed that the methane flux in the SMTZ region could be calculated using Fick's first law (Equations 2, 3; Schulz, 2006).

$$J = -\varphi D_S \partial C / \partial x \quad (2)$$

$$D_S = D_0/(1 - \ln \varphi^2) \quad (3)$$

Where J represents the diffusion flux (mmol m^{-2} yr^{-1}), φ represents the porosity (assuming a porosity of 0.7 for our study area), Ds is the diffusion coefficient for sediment (m^{-2} s^{-1}), C is the concentration of dissolved components (mmol L^{-1}), x represents the sediment depth (m), and D_0 is the diffusion coefficient for seawater (m^{-2} s^{-1}) with a value of 5.72×10^{-10} m^{-2} s^{-1} in this study (Schulz, 2006).

4 Result

4.1 Sediment characteristics

Core YEC7–1 (3.05 m long) is composed primarily of yellowish-gray clayey silt with localized millimeter-scale dark-gray laminae that emit a faint odor (Figure 3A). Grain size distribution is relatively uniform, with an average value of 7.13 Φ. OC content is predominantly between 0.38% and 0.72%, averaging 0.52%. $\delta^{13}C$ values of OC fall within a narrow range, averaging -23.39‰ and spanning from -23.01‰ to -23.84‰.

Core YEC7–2 (2.25 m long) is composed mainly of dark-gray clayey silt (Figure 3B). Grain size shows minimal variation, averaging 7.14 Φ. OC content generally falls within the 0.41% to 0.92% range, with an average of 0.55%. Notably, the upper 20 cm exhibits higher and more variable OC content compared to the more consistent values below 20 cm. The $\delta^{13}C$ values of OC range from -22.89‰ to -23.99‰, with a mean of -23.36‰.

Based on the depth profiles, ^{210}Pbex is present above 46.5 cm and 58.5 cm in core YEC7–1 and YEC7–2, respectively. The logarithmic fitting of ^{210}Pbex reveals relatively high R^2 values of 0.87 and 0.74 in core YEC7–1 and YEC7–2, respectively, indicating relatively stable input of ^{210}Pb in our two cores. Therefore, the constant initial concentration model was applied to derive the sediment rates (SR) (Robbins and Edgington, 1975). The average SR derived from the ^{210}Pbex data are 0.86 cm yr^{-1} for YEC7–1 and 1.26 cm yr^{-1} for YEC7–2.

4.2 Porewater geochemical characteristics

Porewater sulfate (SO_4^{2-}) concentration in core YEC7–1 exhibits a pronounced decrease from near-surface values of 28 mmol L^{-1} to depletion (0 mmol L^{-1}) downcore (Figure 4A). This curve exhibits a upward convex shape between 0 and 80 cm, followed by a near-linear decrease to near-zero values between 80 and 160 cm. Concentrations of calcium (Ca^{2+}) and magnesium (Mg^{2+}) also decrease with depth, while the ratios of Mg^{2+}/Ca^{2+} and Sr^{2+}/Ca^{2+} show a significant downcore increase. Barium (Ba) concentration exhibits a gradual increase down to 120 cm, followed by a more rapid rise until 180 cm, before stabilizing at relatively constant values below this depth. Uranium (U) displays a decreasing trend with depth in the upper portion of the core, characterized by significant fluctuations. Below 160 cm, U concentrations remain low with minimal variation. Manganese (Mn) and vanadium (V) concentrations exhibit a consistent downcore decrease throughout the core.

The trend of methane concentration in core YEC7–1 directly opposes that of porewater SO_4^{2-} concentration (Figure 4A). Methane remains near zero concentration from 0 to 120 cm depth, followed by a rapid rise between 120 and 180 cm. Below 180 cm, methane concentration stabilizes around 0.45 mmol L^{-1} with minor fluctuations. However, due to low methane concentrations in the upper 160 cm, isotope fractionation values were not obtainable for some layers. Below 160 cm, $\delta^{13}C$-CH_4 exhibits relative stability, ranging from approximately -90‰ to -100‰. $\delta^{2}H$-CH_4 shows greater variations in this zone, fluctuating between -160‰ and -240‰.

Porewater SO_4^{2-} concentration in core YEC7–2 exhibits a sharp depletion from 20 mmol L^{-1} to near-zero values within the uppermost 20 cm, followed by relatively constant concentrations at greater depths (Figure 4B). Similarly, Ca^{2+} and Mg^{2+} concentrations show a gradual decrease between 0 and 40 cm before reaching relatively stable values deeper in the core. The ratios of Mg^{2+}/Ca^{2+} and Sr^{2+}/Ca^{2+}, however, increase significantly with depth. Ba^{2+} concentration exhibits a rapid rise within the top 20 cm, followed by a plateau with some fluctuations below this depth. Trends for U, Mn, and V mirror each other, all displaying a rapid decrease in concentration between 0 and 20 cm and remaining relatively constant below this zone.

Methane concentration increases steadily within the upper 80 cm, reaching approximately 1 mmol L^{-1}, and then plateaus (Figure 4B). Notably, $\delta^{13}C$-CH_4 shows a slight downcore depletion, decreasing from -70‰ to -74‰, while $\delta^{2}H$-CH_4 exhibits a subtle enrichment with depth, increasing from -200‰ to -190‰.

4.3 SMI depth and methane diffusive flux

The depth of SMI in core YEC7–1 is estimated 168.8 cm. Using Equation 3, the calculated downward diffusive sulfate flux at YEC7–1 is 73 mmol m^{-2} yr^{-1} (Figure 5A), approximately equal to the upward diffusive methane flux from the SMI. In core YEC7–2, porewater sulfate concentration becomes near-depleted at a depth of 20 cm (Figure 4B). The depth of SMI in core YEC7–2 is estimated 18.4 cm, and the downward diffusive sulfate flux is calculated to be 619 mmol m^{-2} yr^{-1} (Figure 5B), again roughly equivalent to the upward diffusive methane flux from the SMI.

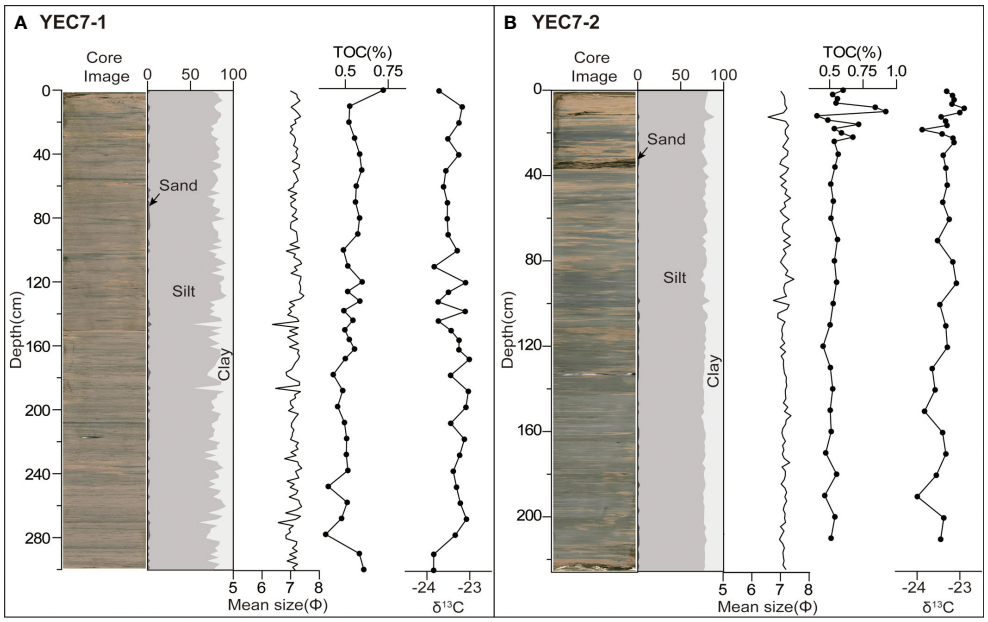

FIGURE 3
Core descriptions of YEC7–1 **(A)** and YEC7–2 **(B)**: photographs, grain-size compositions, mean grain size, total organic carbon (TOC) and $\delta^{13}C$ values of OC.

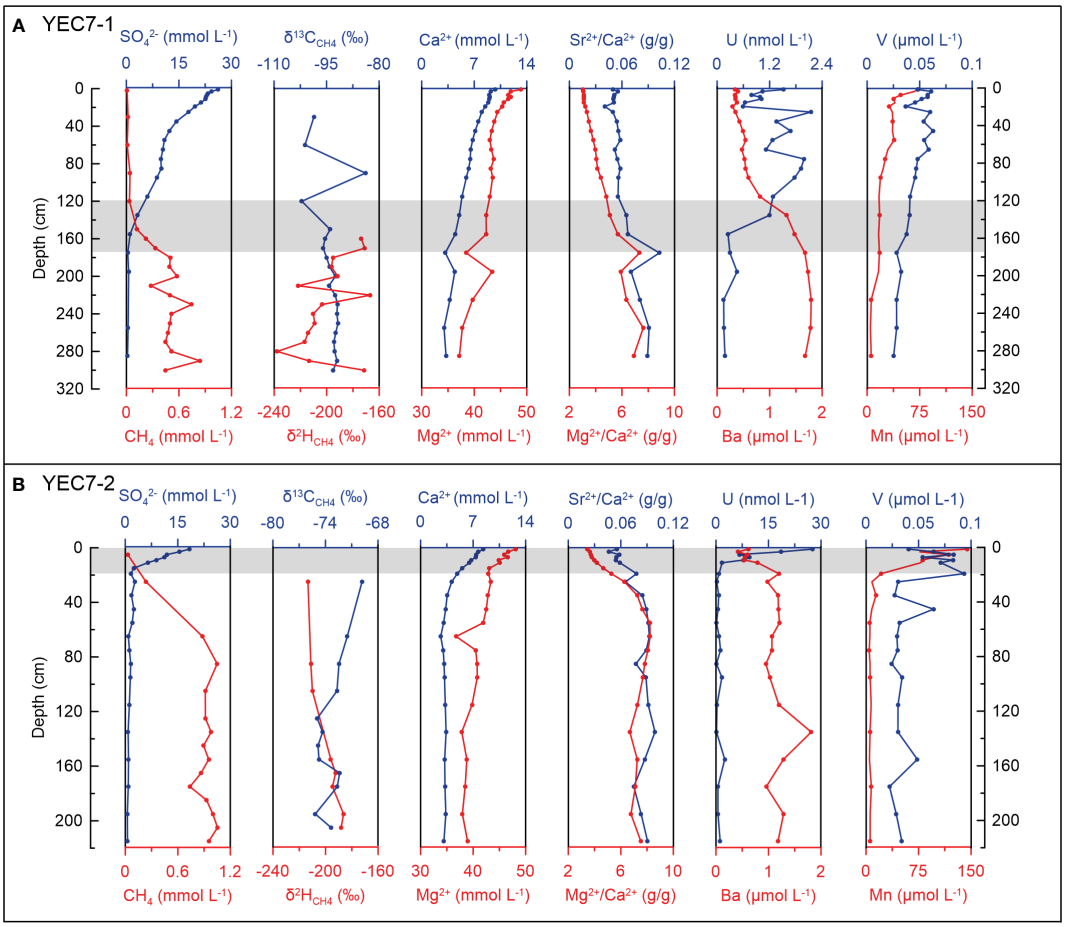

FIGURE 4
Vertical profiles of dissolved components in porewater from cores YEC7–1 **(A)** and YEC7–2 **(B)**. Shaded area represents the SMTZ.

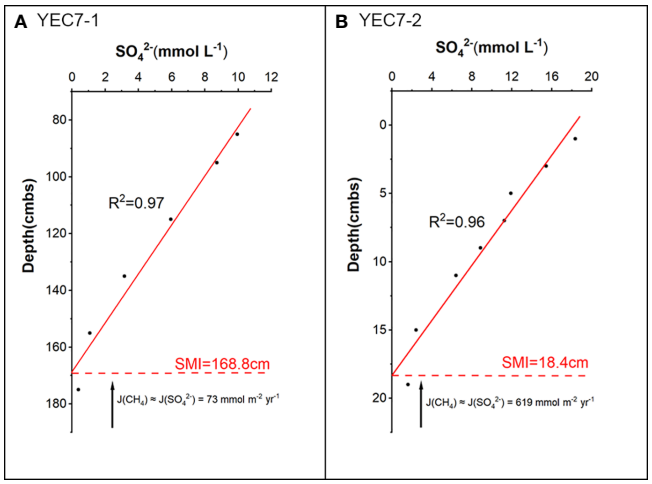

FIGURE 5
Estimated SMI depth and diffusive methane flux in cores YEC7–1 **(A)** and YEC7–2 **(B)**.

5 Discussion

5.1 Variations in the SMTZ burial depth and potential causes

Early diagenesis involves sulfate reduction through two primary pathways: AOM and organoclastic sulfate reduction (OSR). When methane is abundant, AOM becomes the dominant mechanism for sulfate consumption, establishing the SMTZ (Borowski et al., 1996). Conversely, organic matter and dissolved sulfate are most reactive near the sediment surface, driving OSR and the formation of curved, convex-up sulfate profiles because of the ratio of organic matter to sulfate (2:1) (Equation 4; Borowski et al., 1996; Hu et al., 2015).

$$2CH_2O + SO_4^{2-} \rightarrow 2HCO_3^- + H_2S \quad (4)$$

However, high methane fluxes can result in steeper, potentially linear, sulfate profiles and shallower SMTZ depths due to the dominance of AOM (Borowski et al., 1999; Ye et al., 2016; Xu et al., 2018). Consistent with previous observations (Borowski et al., 1996), Figure 5 depicts steep, near-linear sulfate gradients (r^2>95%) in YEC7–1 (80–170 cm) and YEC7–2 (0–20 cm), to support AOM as the dominant process in these intervals. The shallow SMI depths in YEC7–1 (168.8 cm) and YEC7–2 (18.4 cm) support this interpretation, as evidenced by the corresponding high methane fluxes of 73 mmol m^{-2} yr^{-1} and 619 mmol m^{-2} yr^{-1} in the two cores, respectively (Figure 5).

He et al. (2020) reported a deeper SMI depth at 800 cm and a lower methane diffusion flux of 4.65 mmol m^{-2} yr^{-1} in core YS6 from Hangzhou Bay (Figure 6C). In contrast, Figure 6 reveals a gradual decrease in SMI depth from YS6 to YEC7–1 and YEC7–2, accompanied by an anticipated increase methane flux. The factors responsible for these contrasting observations in SMI depth and methane flux are investigated further below.

5.1.1 Sedimentation rates

The ECS is a marginal sea heavily influenced by riverine input (Bi et al., 2015). Zheng et al. (2011) demonstrated that sedimentation rates not only control the type of early diagenetic zone but also its thickness on the ECS shelf. AOM, a key early diagenetic process, corresponds to changes in SMI depth with variations in sedimentation rates. Within the SMTZ, rapid microbial sulfate reduction due to AOM leads to fractionation of multiple sulfur isotopes (Deusner et al., 2014). Recent studies have shown that rapid depositional events within the mud zone of the ECS inner shelf also favored the formation of closed diagenetic environments, and the migration of SMTZ has also been verified by multi-sulfur isotopes (Liu et al., 2019; Chang et al., 2020). Due to abundant terrestrial input and unstable sedimentary dynamics in the ECS shelf (Zhang et al., 2023), sedimentation rates vary significantly over different sites. The sedimentation rates at site YEC7–1 and YEC7–2 in this study are 0.86 cm yr^{-1} and 1.26 cm yr^{-1} (Figure 7), and they were indicated to be slightly higher than YS6 (Figure 8; Wang et al., 2013), but their minor difference should not account for their remarkable difference in SMI depth (Figure 6).

5.1.2 TOC contents

Nutrient-rich, low-salinity coastal environments characterized by high organic matter deposition rates also exhibit shallower SMI depths in sediments (Egger et al., 2015). For example, study has linked decreasing SMI depth in the Baltic Sea to anthropogenic eutrophication (Fleming-Lehtinen et al., 2008). Land-derived nutrient enrichment can stimulate primary production, resulting in more organic matter deposition on the seabed. This increased organic matter load has the potential to drive higher sulfate reduction and methane generation rates, ultimately causing the SMI to become shallower. The Yangtze Estuary, similar to the Baltic Sea, has experienced eutrophication in recent decades due to

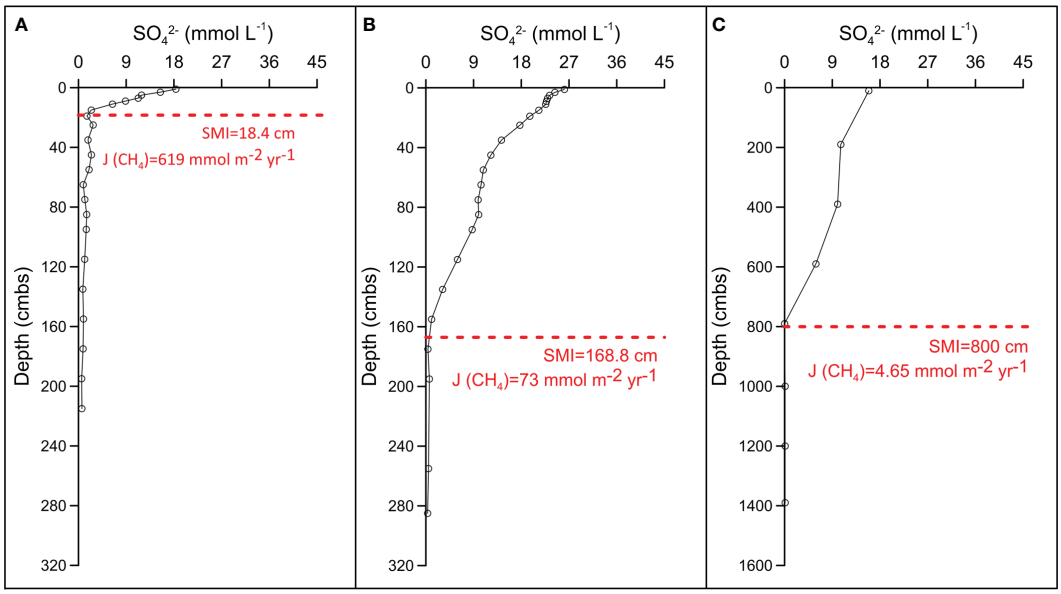

FIGURE 6
Depth profiles of porewater sulfate concentrations, and the derived SMI depths and methane fluxes at YEC7–2 **(A)**, YEC7–1 **(B)**, and YS6 **(C)**. Data for YS6 are reproduced from He et al. (2020). (See Figure 1 for the core location of YS6).

anthropogenic nutrient discharge (Wu et al., 2020). Eutrophication can lead to the expansion of hypoxic zones, favoring anaerobic organic matter mineralization and potentially increasing methane production in bottom sediments. These processes can ultimately cause the SMI to shoal and promote more widespread methane leakage (Naqvi et al., 2010). While Kao et al. (2003) reported higher TOC values (>0.50%) in the Yangtze delta-front, with TOC contents decreasing offshore and downstream, the mean TOC contents at YEC7–1 and YEC7–2 (0.52% and 0.55%, respectively) are sufficient for microbial methane production (Rice and Claypool, 1981). Additionally, the TOC contents of YS6 within Hangzhou Bay is approximately 0.5% (Li et al., 2023), and which observed in Zhoushan Archipelago region, where YEC7–1 and YEC7–2 are located, are comparable to YS6. Therefore, the shallower SMI depths in YEC7–1 and YEC7–2 compared to YS6 in Hangzhou Bay (Figure 6) cannot be solely attributed to differences in organic matter content and associated methane generation.

5.1.3 Changing gas front in the Holocene sediments

Organic carbon (OC) burial flux is typically considered a major control on sulfate consumption and, consequently, the depth of the SMI (Canfield, 1991). However, the substantial difference in SMI depth observed between YEC7–1 and YEC7–2 (separated by only 373.5m) challenges this paradigm. The similarity in sediment characteristics between these cores (Figure 3) further suggests that

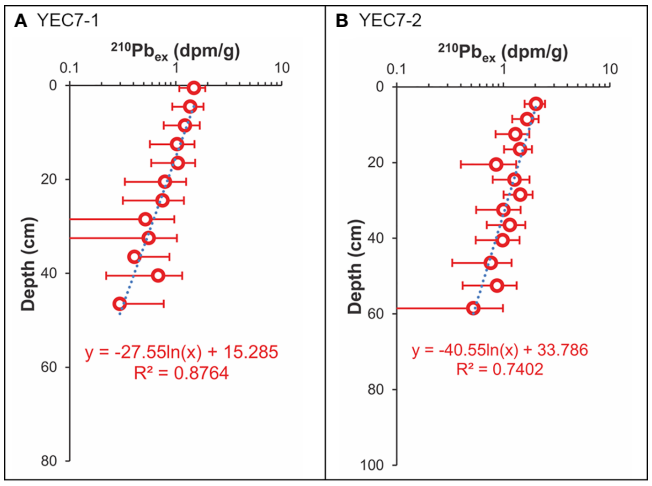

FIGURE 7
Depth profiles of $^{210}Pb_{ex}$ in sediment at cores YEC7–1 **(A)** and YEC7–2 **(B)**.

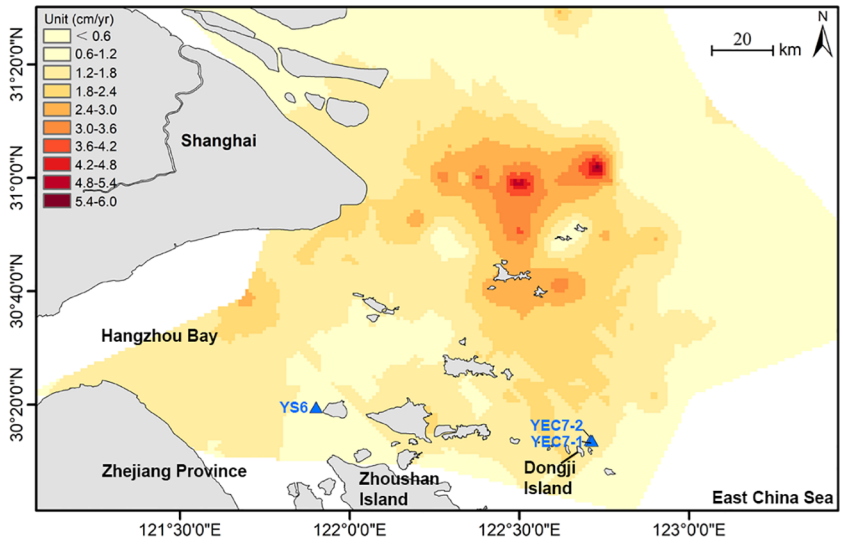

FIGURE 8
Spatial distribution of sedimentation rates in the Yangtze Delta, Hangzhou Bay, and the ECS inner shelf (data from Wang et al., 2013).

OC burial flux alone cannot explain the observed variation in SMI depth. Supporting observations come from studies in the Hola region, where despite cores showing similar sediment grain size and organic matter composition, SMI depth exhibited substantial variations within a small area (Borowski et al., 1996; Hensen et al., 2003). These findings suggest that variations in the upward flux of CH_4 from buried shallow gas in the Holocene sediments might be a key factor influencing SMI depth. Notably, the estimated CH_4 flux at YEC7–2 is 8.5 times higher than that at YEC7–1 (Figure 5).

The sub-bottom profile near YEC7–2 reveals distinct acoustic blanking zones, indicative of shallow gas within the Holocene sediments (Figure 9; Yang et al., 2021). The upper boundary of the acoustic blanking zone was termed a "gas front" by Judd and Hovland (2007). The depth of the gas front further influences the depth of the SMI through controlling the methane diffusion flux. A shallower gas front allows for a greater upward diffusive flux of methane, ultimately causing an upward shift of the SMTZ (Mogollón et al., 2013; Flury et al., 2016). Studies have shown that the gas front depth in Hangzhou Bay is shallower than that in the Yangtze subaqueous delta, with both reaching depths no greater than 17.5 m (Song et al., 2023). In some locations, the cap overlying shallow gas is very thin, and the presence of pockmarks on the seabed further suggests active gas seepage. Our July 2022 cruise also captured evidence of gas bubbles emanating from the seabed near YEC7–2 using the multibeam echosounder. Based on these observations, we attribute the shallower depth of the SMI at YEC7–2 to active gas seepage (Figure 2B). While active seepage was not directly observed at YEC7–1 during the cruise, its close proximity to YEC7–2 (only 373.5m away) raises the possibility that it may also be influenced by gas seepage from nearby.

5.2 Evidences of methane leakage from porewater geochemical compositions

Geophysical methods can offer direct evidence for shallow gas activities such as outflowing of gas bubbles from the pockmarks but leakage events are not easily caught by infrequent cruise surveys (Figure 2), while methane leakages should leave some clues in porewater and sediment geochemistry, serving as reliable proxies for reconstructing their past activities. The AOM within the SMTZ releases significant amounts of H_2S, intensifying reducing conditions in the early diagenetic environment. This, in turn, affects the behavior of redox-sensitive elements within the sediments (Peketi et al., 2015). When methane leaks from the Holocene gassy sediments, it undergoes microbially mediated reactions with various porewater components. These reactions not only affect the ionic composition of the porewater but also influence the formation of authigenic minerals (Bayon et al., 2011; Liu et al., 2020b).

5.2.1 The response of porewater trace element distributions to methane leakages

Early diagenesis is characterized by a gradual shift from aerobic conditions at the sediment surface to suboxic and ultimately anoxic conditions with increasing depth (Deng et al., 2020; Smrzka et al., 2020). This changing redox environment influences the behavior of various trace elements. Notably, U and V are typically reduced and enriched during denitrification, while Ni, Co, Cu, Zn, Cd, and Mo primarily accumulate under sulfate-reducing conditions in sediment (Tribovillard et al., 2006), and the enrichment of these elements in pore water is exactly the opposite. By exploiting these contrasting behaviors, we can utilize their distribution patterns to infer the dominant redox conditions within specific sedimentary systems.

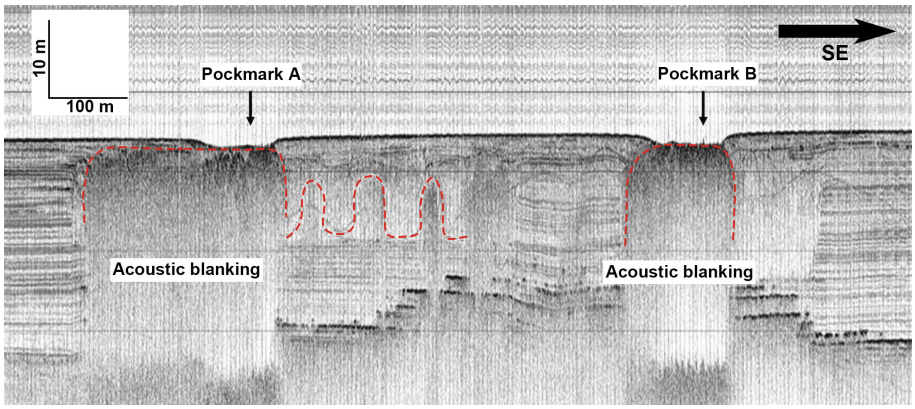

FIGURE 9
Sub-bottom profile near YEC7–1 and YEC-2 showing gas seepages and associated pockmarks on the seabed (Modified from Yang et al., 2021). Gas front marked in the red dashed line.

U, highly sensitive to redox processes, is a key element for reconstructing fluctuations in bottom-water oxygen content (McManus et al., 2006; Algeo and Tribovillard, 2009). The elevated uranium (U) concentrations observed in the porewater at the surface sediments of YEC7–1 and YEC7–2 (Figure 4) are consistent with oxidizing conditions prevailing during the early stages of diagenesis. However, the high methane diffusive flux at YEC7–2 likely triggered a sharp decrease in U concentration at the SMTZ. This suggests a rapid shift from oxidizing to reducing conditions driven by methane consumption. In contrast, porewater U concentrations in YEC7–1 exhibit fluctuations above the SMTZ, potentially reflecting biological activity in surface sediments, but remain generally higher. The early diagenetic environment progresses to reducing conditions as expected following the SMTZ. Methane leakage likely strengthens the local reducing environment, potentially hindering the occurrence of certain oxidative reactions.

The upper layers (0–80 cm) of YEC7–1 display co-occurring peaks in V and U concentrations (Figure 4). This phenomenon aligns with enhanced OSR. As organic matter decomposes, chelated metal elements are released into the porewater (McManus et al., 2005; Miao et al., 2022), leading to elevated concentrations of specific heavy metal ions like V. Porewater Mn concentration also exhibits enrichment within the 0–80 cm interval, consistent with the "reduction of iron-manganese oxides" stage in the classical early diagenetic zonation model (De Schamphelaire et al., 2007). High Mn concentrations at the top of different cores likely reflect a higher terrestrial input (Canfield, 1989). Mn concentrations remain relatively stable between 20–60 cm, but decrease steadily below 60 cm, following the expected pattern for early diagenesis. V typically exists in dissolved form under oxidizing conditions, but reacts with H_2S and precipitates into sediments under reducing conditions (Algeo and Maynard, 2004; Algeo and Li, 2020). At YEC7–1, decreasing V concentrations with depth reflect the transition from oxidizing to reducing conditions.

The high methane leakage flux at YEC7–2 is reflected in the porewater Mn profile. Mn concentration exhibits a peak at the seawater-sediment interface, followed by a sharp decline within the upper 30 cm and remains stable thereafter. This rapid shift suggests a swift transition from oxidizing to reducing conditions at this depth, with Mn likely precipitating as authigenic minerals (Lovley, 1991; Zopfi et al., 2008). Furthermore, consistent with the preferential enrichment of V under reducing conditions, V concentration shows a rapid decrease to a steady value below 20 cm.

5.2.2 The response of authigenic minerals to methane seepage as shown by changes in porewater ion concentrations and ratios

Methane leakage can significantly impact geochemical processes within seafloor sediments, including the formation of authigenic minerals such as carbonate (calcite, high-Mg calcite) and barite. The precipitation of authigenic carbonates during early diagenesis is a crucial process in reducing carbon flux to the water column. Typically, the increase in bicarbonate and hydrogen sulfide generated by OSR and AOM enhances porewater alkalinity, facilitating the rapid precipitation of authigenic carbonates (Bayon et al., 2007; Feng et al., 2018).

Authigenic carbonate formation necessitates sufficient alkalinity, provided by the HCO_3^- generated during AOM (Naehr et al., 2007). Decreasing concentrations of porewater alkaline earth metals (Mg^{2+}, Ca^{2+}, and Sr^{2+}) with depth in YEC7–1 and YEC7–2 suggest precipitation of authigenic carbonates as similar patterns discussed by Hu et al. (2015) and Xu et al. (2018). At YEC7–1, porewater Ca^{2+} and Mg^{2+} concentrations exhibit a depth-dependent decline throughout the core (Figure 4A), indicative of rapid carbonate precipitation (Dwyer et al., 2000). Concurrently, the Mg^{2+}/Ca^{2+} and Sr^{2+}/Ca^{2+} ratios in porewater increase significantly with depth. This suggests a higher Sr^{2+}/Ca^{2+} ratio in the authigenic carbonates compared to seawater (Figure 10). Since aragonite has a higher Sr^{2+}/Ca^{2+} ratio than seawater, its precipitation lowers the porewater Sr^{2+}/Ca^{2+} ratio. Conversely, high-Mg calcite precipitation increases the porewater Sr^{2+}/Ca^{2+} ratio (Nöthen and Kasten, 2011). Therefore, we infer that the sedimentary carbonates at YEC7–1 and YEC7–2 are high-Mg calcite precipitation. Additionally, high-Mg calcite precipitation formation is favored in sediments with lower sulfate

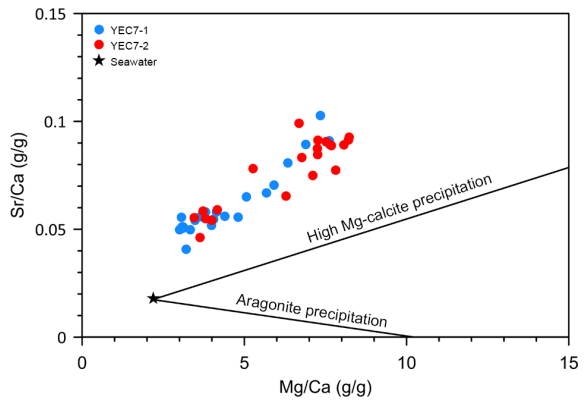

FIGURE 10
Plot of Sr/Ca vs. Mg/Ca (weight ratios) in the porewater. The Sr/Ca and Mg/Ca ratios of the precipitating aragonite and high Mg-calcite as well as seawater were taken from Bayon et al. (2007) and Nöthen and Kasten (2011).

concentrations and methane flux compared to aragonite (Feng et al., 2016; Chen et al., 2021).

In marine sediments, Ba primarily resides in aluminosilicates, iron-manganese (hydro)oxides, or barite due to its low solubility. In regions where AOM occurs, the sulfate concentration in porewater is low, which promotes the dissolution of barite, thereby releasing a large amount of Ba^{2+} into the porewater (Feng and Roberts, 2011). This phenomenon is evident in YEC7–1 and YEC7–2 (Figure 4), where Ba^{2+} concentrations exhibit an opposing trend to sulfate concentrations. Biogenic barium, a common productivity proxy (Dymond et al., 1992; Hu et al., 2015), is typically measured alongside other geochemical indicators like nutrient concentrations. However, the observed barite dissolution coinciding with decreasing sulfate concentrations (Figure 4) suggests a potential underestimation of paleoceanic primary productivity using barite content. Furthermore, intensified methane leakage may further complicate the reconstruction of paleo-productivity in the ECS inner shelf (Li et al., 2018; Miao et al., 2022).

5.3 Variations in methane leakage flux and potential causes

Continental margins experience methane leakage primarily through diffusion, with fluxes ranging from 0.05 to 800 mmol m^{-2} yr^{-1}, with an average of 100 mmol m^{-2} yr^{-1} (Regnier et al., 2011). The sulfate-methane consumption balance method estimated fluxes of 73 mmol m^{-2} yr^{-1} at YEC7–1 and 619 mmol m^{-2} yr^{-1} at YEC7–2 (Figure 5). Furthermore, methane fluxes could be significantly higher near pockmarks, where visible gas bubbles emanated from the seabed near YEC7–2 (Figure 2).

5.3.1 The formation and migration of shallow gas

In marine environments, methane can originate from two primary sources: the thermocatalytic decomposition of complex organic matter at temperatures above 150°C (thermogenic methane) and methanogenic bacteria activity at temperatures below 80°C (microbial methane) (Clayton, 1991). The isotopic composition of methane serves as an effective tool for differentiating its origin (Figure 11). Microbial methane isotopic composition ($\delta^{13}C$-CH_4) is closely related to active methane-producing populations, with $\delta^{13}C$ ranging between -110‰ and -50‰ (Whiticar et al., 1986; Whiticar, 1999). Thermogenic methane typically has heavier $\delta^{13}C$-CH_4 signature, ranging from -50‰ to -20‰ (Schoell, 1988; Whiticar, 1999). Whiticar (1999) proposed a schematic diagram for identifying methane sources based on $\delta^{13}C$-CH_4 and $\delta^{2}H$-CH_4 compositions (Figure 11). Isotopic analysis of methane from YEC7–1 and YEC7–2 indicates a microbial source, likely produced through bacterial carbonate reduction (Figure 11). The heavier $\delta^{13}C$-CH_4 (-70‰ to -80‰) at YEC7–2 than YEC7–1 (-90‰ to -100‰) could be attributed to larger methane fluxes and/or the mixing of some thermogenic methane with microbial methane during migration at YEC7–2. The former factor seems confirmed by the methane flux estimations (Figure 5), but the latter needs more clues for potential isotope fractionation over different distance migration.

5.3.2 Increasing methane leakage triggered by seabed erosion

More frequent occurrences of methane leakage in shelf seas have recently been reported due to natural and anthropogenic disturbances, attracting broad attention because of its highly efficient contribution to global warming (Reeburgh, 2007; Rhee et al., 2009; Letcher, 2019). Seafloor erosion triggered by storm events or sediment deficit could disturb the stability of burial shallow gas in the Holocene sediments, leading to strong gas leakage events or slow but sustained gas leakages, respectively. The construction of thousands of dams within the Yangtze River catchment in recent decades has significantly reduced sediment discharge into the East China Sea. Sediment flux decreased dramatically from 430 mt yr^{-1} (1952–2002) to 140 mt yr^{-1} (2003–2016) following the completion of the TGD in 2003 (Fan et al., 2017). Due to sediment deficit, seafloor erosion has been widely reported in the Yangtze subaqueous delta (Yang et al., 2011; Guo et al., 2021), and has recently extended into Hangzhou Bay (Xie et al., 2013, 2017). The seafloor erosion has been accused of increasing gas leakage in the Yangtze subaqueous delta (Chen et al., 2020) and Hangzhou Bay (Song et al., 2023). They further pointed out the mutual promotion effect between seafloor erosion and gas leakage at local scales (Chen et al., 2020; Song et al., 2023).

The seafloor erosion has been less studied in the ECS inner shelf due to shortage of bathymetric data, but it should have occurred based on therein decreasing suspended sediment concentrations and longshore sediment fluxes (Deng et al., 2017). Very thin cap of shallow gas with the presence of pockmarks near YEC7–2 (Figure 9) could link with recent development of seafloor erosion (Yang et al., 2021). Under accretion or weak erosion stage, shallow gas can be capped by thick strata to stay stably below modern SMTZ interval, resulting in a regular early diagenesis profile from oxic, through to suboxic and sulfidic, to SMTZ subzones as shown in YS6 (Figure 12A). Continued seafloor erosion can lead to decreasing

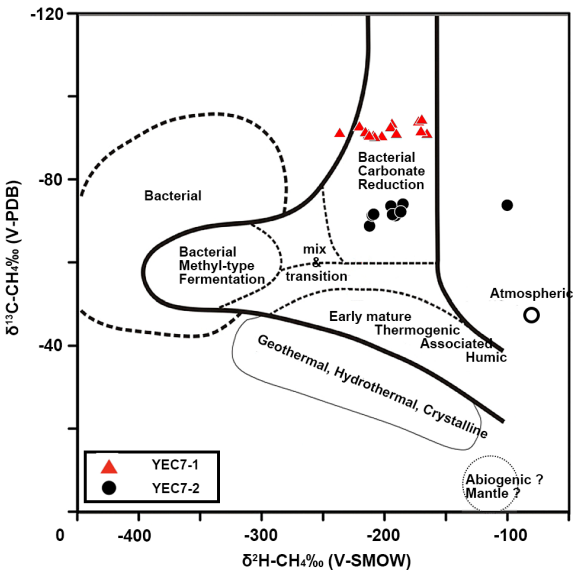

FIGURE 11
Distinguishing methane sources based on $\delta^{13}C$-CH_4 and $\delta^{2}H$-CH_4 compositions (modified from Whiticar et al., 1986).

cap pressure, potentially causing the shallowing of the SMTZ depth and a thinning of the early diagenetic profile observed in YEC7–1. This scenario might also result in occasional gas leakage through fractured zones in the sediment (Figure 12B). When the mutual promotion between subfloor erosion and gas leakage occurs, strong impact by gas leakage significantly modifies the early diagenesis profile with the uplifted SMTZ depth toward the seafloor as shown in YEC7–2, where pockmarks are well developed with gas outflow into the seawater in terms of bubbles (Figure 12C). Massive methane leakage can trigger submarine landslides, and the released methane contributes to global warming, ocean acidification, and even potential mass extinctions. These chain actions are still less known, deserving more attention due to their adverse environmental impacts (Reeburgh, 2007; Rhee et al., 2009; Letcher, 2019; Chen et al., 2020; Song et al., 2023).

6 Conclusion

Two short cores were collected in the muddy inner shelf of the East China Sea with significant impact of gas leakages. Sediment and porewater geochemical analyses show that early diagenesis in both cores have been remarkably influenced by methane leakages. The core YEC7–2 has a higher uplifted SMTZ interval than YEC7–1 because the former is located very close to a pockmark with active methane leakage into the seawater and the latter is located 373.5m away. This is further corroborated by the large difference in the estimated methane diffusive fluxes which is 619 mmol m^{-2} yr^{-1} at YEC7–2, roughly 8.5 times that at YEC7–1 (73 mmol m^{-2} yr^{-1}). Moreover, heavier $\delta_{13}C$-CH4 (-70‰ to -80‰) at YEC7–2 than that (-90‰ to -100‰) at YEC7–1 gives another clue to larger methane fluxes at YEC7–2. Increasing occurrences of methane leakages mainly result from sediment deficit due to huge amounts of dams been recently constructed in the Yangtze drainage basin.

Methane leakages have obviously changed early diagenesis processes as shown by the SMTZ shifting and SMI depth variations in porewater geochemistry. Elevated U, V and Mn concentrations in porewater were observed within and above the SMI, but sharply declining below the SMI in response to downcore change from oxic/suboxic to reductive conditions. Downcore decrease in concentrations of Mg^{2+}, Ca^{2+}, and Sr^{2+} demonstrate precipitation of authigenic carbonates, and downcore increase in Mg^{2+}/Ca^{2+} and Sr^{2+}/Ca^{2+} ratios hint authigenic carbonates been predominated by aragonite. Schematic models are therefore developed to show changing early diagenesis profiles in response

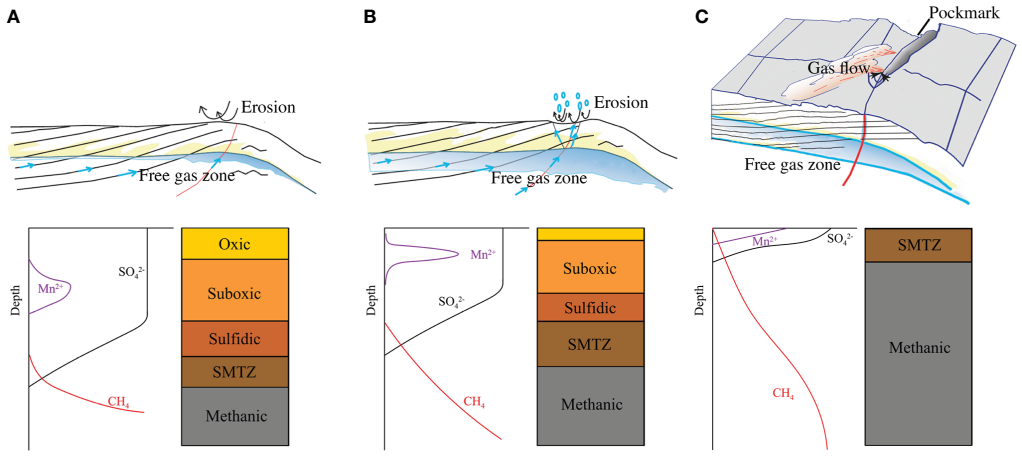

FIGURE 12
Methane leakage development stages and their associated early diagenesis patterns. **(A)** Accretion or weak seafloor erosion with deep burial gas front in the Holocene Sediments, and a regular early diagenesis profile in the recent sediments with deep SMTZ interval; **(B)** Increased seafloor erosion to trigger weak gas leakage, consequently induced the up-lifted SMTZ interval; **(C)** Severe seafloor erosion at pockmarks where strong gas leakage occurs with the highly up-lifted SMTZ toward the seafloor (after Bangs et al., 2010; Aller, 2014).

to little, weak and strong methane leakages from the Holocene gassy sediments under different sedimentation states from accretion, through to slight erosion, and to severe erosion with pockmarks.

Data availability statement

The original contributions presented in the study are included in the article/Supplementary Material, further inquiries can be directed to the corresponding author/s.

Author contributions

CW: Investigation, Writing – original draft. JS: Funding acquisition, Writing – review & editing. SL: Writing – review & editing. PQ: Data curation, Writing – review & editing. DF: Funding acquisition, Supervision, Writing – review & editing.

Funding

The author(s) declare financial support was received for the research, authorship, and/or publication of this article. This study was supported by the National Natural Science Foundation of China (NSFC- 42330411, 42206062), the Open Foundation of Zhoushan Field Scientific Observation and Research Station for Marine Geo-hazards, China Geological Survey (ZSORS-22-11), and the Innovation Program of Shanghai Municipal Education Commission (2021-01-07-00-07-E00093).

Conflict of interest

The authors declare that the research was conducted in the absence of any commercial or financial relationships that could be construed as a potential conflict of interest.

Publisher's note

Supplementary material

The Supplementary Material for this article can be found online at: https://www.frontiersin.org/articles/10.3389/fmars.2024.1410241/full#supplementary-material

References

Algeo, T. J., and Li, C. (2020). Redox classification and calibration of redox thresholds in sedimentary systems. *Geochim. Cosmochim. Acta* 287, 8–26. doi: 10.1016/j.gca.2020.01.055

Algeo, T. J., and Maynard, J. B. (2004). Trace-element behavior and redox facies in core shales of Upper Pennsylvanian Kansas-type cyclothems. *Chem. Geol.* 206, 289–318. doi: 10.1016/j.chemgeo.2003.12.009

Algeo, T. J., and Tribovillard, N. (2009). Environmental analysis of paleoceanographic systems based on molybdenum-uranium covariation. *Chem. Geol.* 268, 211–225. doi: 10.1016/j.chemgeo.2009.09.001

Aller, R. C. (2014). "Sedimentary diagenesis, depositional environments, and benthic fluxes," in *Treatise on geocbemistry, vol. 8: the oceans and marine geocbemistry*. Eds. M. J. Mottl and H. Elderfield (Amsterdam: Elsevier), 293–334.

Bange, H. W., Bartell, U. H., Rapsomanikis, S., and Andreae, M. O. (1994). Methane in the Baltic and North Seas and a reassessment of the marine emissions of methane. *Glob. Biogeochem. Cycles.* 8, 465–480. doi: 10.1029/94gb02181

Bangs, N. L., Hornbach, M. J., Moore, G. F., and Park, J. O. (2010). Massive methane release triggered by seafloor erosion offshore southwestern japan. *Geology* 38 (11), 1019–1022. doi: 10.1130/G31491.1

Bayon, G., Birot, D., Ruffine, L., Caprais, J.-C., Ponzevera, E., Bollinger, C., et al. (2011). Evidence for intense REE scavenging at cold seeps from the Niger Delta margin. *Earth Planet. Sci. Lett.* 312, 443–452. doi: 10.1016/j.epsl.2011.10.008

Bayon, G., Pierre, C., Etoubleau, J., Voisset, M., Cauquil, E., Marsset, T., et al. (2007). Sr/Ca and Mg/Ca ratios in Niger Delta sediments: Implications for authigenic carbonate genesis in cold seep environments. *Mar. Geol.* 241, 93–109. doi: 10.1016/j.margeo.2007.03.007

Bi, L., Yang, S., Li, C., Guo, Y., Wang, Q., Liu, J. T., et al. (2015). Geochemistry of river-borne clays entering the East China Sea indicates two contrasting types of weathering and sediment transport processes. *Geochem. Geophys. Geosyst.* 16, 3034–3052. doi: 10.1002/2015gc005867

Boetius, A., Ravenschlag, K., Schubert, C. J., Rickert, D., Widdel, F., Gieseke, A., et al. (2000). A marine microbial consortium apparently mediating anaerobic oxidation of methane. *Nature* 407, 623–626. doi: 10.1038/35036572

Boetius, A., and Wenzhöfer, F. (2013). Seafloor oxygen consumption fuelled by methane from cold seeps. *Nat. Geosci.* 6, 725–734. doi: 10.1038/ngeo1926

Borowski, W. S., Paull, C. K., and Ussler, W. (1996). Marine pore-water sulfate profiles indicate in *situ* methane flux from underlying gas hydrate. *Geology* 24, 655–658. doi: 10.1130/0091–7613(1996)024<0655:MPWSPI>2.3.CO;2

Borowski, W. S., Paull, C. K., and Ussler, W. (1999). Global and local variations of interstitial sulfate gradients in deep-water, continental margin sediments: Sensitivity to underlying methane and gas hydrates. *Mar. Geol.* 159, 131–154. doi: 10.1016/S0025–3227(99)00004–3

Canfield, D. E. (1989). Reactive iron in marine sediments. *Geochim. Cosmochim. Acta* 53, 619–632. doi: 10.1016/0016–7037(89)90005–7

Canfield, D. E. (1991). Sulfate reduction in deep-sea sediments. *Am. J. Sci.* 291 (2), 177–188. doi: 10.2475/ajs.291.2.177

Cathles, L. M., Su, Z., and Chen, D. (2010). The physics of gas chimney and pockmark formation, with implications for assessment of seafloor hazards and gas sequestration. *Mar. Pet. Geol.* 27, 82–91. doi: 10.1016/j.marpetgeo.2009.09.010

Chang, X., Zhang, M., Gu, Y., Wang, H., and Liu, X. (2020). Formation mechanism and controlling factors of authigenic pyrite in mud sediments on the shelf of the yellow sea and the East China sea. *Adv. Earth Sci.* 35, 1306. doi: 10.11867/j.issn.1001–8166.2020.105

Chen, Q., Zhang, H., and Cui, Y. (2008). The potential shallow gas disasters and its prevention measures surrounding. *Shanghai. Sea.* 01), 8–12.

Chen, T., Sun, X., Lin, Z., Lu, Y., Fang, Y., Wu, Z., et al. (2021). Deciphering the geochemical link between seep carbonates and enclosed pyrite: A case study from the northern South China sea. *Mar. Pet. Geol.* 128, 105020. doi: 10.1016/j.marpetgeo.2021.105020

Chen, Y., Deng, B., and Zhang, J. (2020). Shallow gas in the Holocene mud wedge along the inner East China Sea shelf. *Mar. Pet. Geol.* 114, 104233. doi: 10.1016/j.marpetgeo.2020.104233

Clayton, C. (1991). Carbon isotope fractionation during natural gas generation from kerogen. *Mar. Pet. Geol.* 8, 232–240. doi: 10.1016/0264–8172(91)90010-x

Deng, Y., Chen, F., Hu, Y., Guo, Q., Cao, J., Chen, H., et al. (2020). Methane seepage patterns during the middle Pleistocene inferred from molybdenum enrichments of seep

carbonates in the South China Sea. *Ore. Geol. Rev.* 125, 103701. doi: 10.1016/j.oregeorev.2020.103701

Deng, B., Wu, H., Yang, S., and Zhang, J. (2017). Longshore suspended sediment transport and its implications for submarine erosion off the Yangtze River Estuary. *Estuar. Coast. Shelf. Sci.* 190, 1–10. doi: 10.1016/j.ecss.2017.03.015

De Schamphelaire, L., Rabaey, K., Boon, N., Verstraete, W., and Boeckx, P. (2007). Minireview: the potential of enhanced manganese redox cycling for sediment oxidation. *Geomicrobiol. J.* 24, 547–558. doi: 10.1080/01490450701670137

Deusner, C., Holler, T., Arnold, G. L., Bernasconi, S. M., Formolo, M. J., and Brunner, B. (2014). Sulfur and oxygen isotope fractionation during sulfate reduction coupled to anaerobic oxidation of methane is dependent on methane concentration. *Earth Planet. Sci. Lett.* 399, 61–73. doi: 10.1016/j.epsl.2014.04.047

Dwyer, G. S., Cronin, T. M., Baker, P. A., and Rodriguez-Lazaro, J. (2000). Changes in North Atlantic deep-sea temperature during climatic fluctuations of the last 25,000 years based on ostracode Mg/Ca ratios. *Geochem. Geophys. Geosyst.* 1, 1028. doi: 10.1029/2000gc000046

Dymond, J., Suess, E., and Lyle, M. (1992). Barium in deep-sea sediment: A geochemical proxy for paleoproductivity. *Paleoceanography* 7, 163–181. doi: 10.1029/92pa00181

Egger, M., Rasigraf, O., Sapart, C. J., Jilbert, T., Jetten, M. S. M., Röckmann, T., et al. (2015). Iron-mediated anaerobic oxidation of methane in brackish coastal sediments. *Environ. Sci. Technol.* 49, 277–283. doi: 10.1021/es503663z

Fan, D., Shang, S., Cai, G., and Tu, J. (2015). Distinction and grain-size characteristics of intertidal heterolithic deposits in the middle Qiantang Estuary (East China Sea). *Geo-Mar. Lett.* 35, 161–174. doi: 10.1007/s00367–015-0398–2

Fan, D., Wu, Y., Zhang, Y., Burr, G., Huo, M., and Li, J. (2017). South Flank of the Yangtze Delta: Past, present, and future. *Mar. Geol.* 392, 78–93. doi: 10.1016/j.margeo.2017.08.015

Feng, D., Peng, Y., Bao, H., Peckmann, J., Roberts, H. H., and Chen, D. (2016). A carbonate-based proxy for sulfate-driven anaerobic oxidation of methane. *Geology* 44, 999–1002. doi: 10.1130/G38233.1

Feng, D., and Roberts, H. H. (2011). Geochemical characteristics of the barite deposits at cold seeps from the northern Gulf of Mexico continental slope. *Earth Planet. Sci. Lett.* 309, 89–99. doi: 10.1016/j.epsl.2011.06.017

Feng, J., Yang, S., Liang, J., Fang, Y., He, Y., Luo, M., et al. (2018). Methane seepage inferred from the porewater geochemistry of shallow sediments in the Beikang Basin of the southern South China Sea. *J. Asian Earth Sci.* 168, 77–86. doi: 10.1016/j.jseaes.2018.02.005

Fleischer, P., Orsi, T. H., Richardson, M. D., and Anderson, A. L. (2001). Distribution of free gas in marine sediments: a global overview. *Geo-Mar. Lett.* 21, 103–122. doi: 10.1007/s003670100072

Fleming-Lehtinen, V., Laamanen, M., Kuosa, H., Haahti, H., and Olsonen, R. (2008). Long-term development of inorganic nutrients and chlorophyll α in the open northern baltic sea. *Ambio* 37, 86–92. doi: 10.1579/0044–7447(2008)37[86:ldoina]2.0.co;2

Flury, S., Røy, H., Dale, A. W., Fossing, H., Tóth, Z., Spiess, V., et al. (2016). Controls on subsurface methane fluxes and shallow gas formation in Baltic Sea sediment (Aarhus Bay, Denmark). *Geochim. Cosmochim. Acta* 188, 297–309. doi: 10.1016/j.gca.2016.05.037

Gong, G.-C., Wen, Y.-H., Wang, B.-W., and Liu, G.-J. (2003). Seasonal variation of chlorophyll a concentration, primary production and environmental conditions in the subtropical East China Sea. *Deep. Sea. Res. Part II. Top. Stud. Oceanogr.* 50, 1219–1236. doi: 10.1016/s0967–0645(03)00019–5

Guo, X., Yan, X., Zheng, S., Wang, H., and Yin, P. (2021). Characteristics of high-resolution subaqueous micro-topography in the Jinshan Deep Trough and its implications for riverbed deformation, Hangzhou Bay, China. *Estuar. Coast. Shelf. Sci.* 250, 107147. doi: 10.1016/j.ecss.2020.107147

Haroon, M. F., Hu, S., Shi, Y., Imelfort, M., Keller, J., Hugenholtz, P., et al. (2013). Anaerobic oxidation of methane coupled to nitrate reduction in a novel archaeal lineage. *Nature* 500, 567–570. doi: 10.1038/nature12375

He, X., Tan, L., Duan, X., Yin, P., Xie, Y., Yang, L., et al. (2020). Carbon cycle within the sulfate-methane transition zone in the marine sediments of Hangzhou Bay. *Mar. Geol. Quat. Geol.* 40, 51–60. doi: 10.16562/j.cnki.0256–1492.2020021401

Hensen, C., Zabel, M., Pfeifer, K., Schwenk, T., Kasten, S., Riedinger, N., et al. (2003). Control of sulfate pore-water profiles by sedimentary events and the significance of anaerobic oxidation of methane for the burial of sulfur in marine sediments. *Geochim. Cosmochim. Acta* 67, 2631–2647. doi: 10.1016/s0016–7037(03)00199–6

Hu, Y., Feng, D., Liang, Q., Xia, Z., Chen, L., and Chen, D. (2015). Impact of anaerobic oxidation of methane on the geochemical cycle of redox-sensitive elements at cold-seep sites of the northern South China Sea. *Deep. Sea. Res. Part II. Top. Stud. Oceanogr.* 122, 84–94. doi: 10.1016/j.dsr2.2015.06.012

Hu, X., Gu, Z., Zhang, X., Zhao, L. H., and Xing, Z. H. (2016). Seismic shape features and distribution of shallow gas in the sea area off the Yangtze River Estuary. *Mar. Geol. Quat. Geol.* 36, 151–157. doi: 10.16562/j.cnki.0256–1492.2016.01.015

Jiao, N., Zhang, Y., Zeng, Y., Gardner, W. D., Mishonov, A. V., Richardson, M. J., et al. (2007). Ecological anomalies in the east China sea: impacts of the three gorges dam? *Water Res.* 41, 1287–1293. doi: 10.1016/j.watres.2006.11.053

Judd, A., and Hovland, M. (2007). "Seabed fluid flow," in *The impact on geology, biology, and the marine environment*. (Cambridge University Press), 475.

Kao, S. J., Lin, F. J., and Liu, K. K. (2003). Organic carbon and nitrogen contents and their isotopic compositions in surficial sediments from the East China Sea shelf and the southern Okinawa Trough. *Deep. Sea. Res. Part II. Top. Stud. Oceanogr.* 50, 1203–1217. doi: 10.1016/s0967–0645(03)00018–3

Knittel, K., and Boetius, A. (2009). Anaerobic oxidation of methane: progress with an unknown process. *Annu. Rev. Microbiol.* 63, 311–334. doi: 10.1146/annurev.micro.61.080706.093130

Letcher, T. M. (2019). "Why do we have global warming?," in *Managing global warming* (Academic Press), 3–15. doi: 10.1016/B978–0-12–814104–5.00001–6

Li, D.-W., Chang, Y.-P., Li, Q., Zheng, L., Ding, X., and Kao, S.-J. (2018). Effect of sea-level on organic carbon preservation in the Okinawa Trough over the last 91 kyr. *Mar. Geol.* 399, 148–157. doi: 10.1016/j.margeo.2018.02.013

Li, P., Du, J., Liu, L. J., Cao, C. X., and Xu, Y. Q. (2010). Distribution characteristics of the shallow gas in Chinese offshore seabed. *Chin. J. Geol. Hazard. Control.* 21, 69–74. doi: 10.16031/j.cnki.issn.1003–8035.2010.01.036

Li, F., Duan, X., He, X., Zhang, Y., Ying, P., Xie, Y., et al. (2023). Vertical distribution and controlling factors of methane in sediments of Hangzhou Bay. *Mar. Geol. Quat. Geol.* 43, 112–121. doi: 10.16562/j.cnki.0256–1492.2022091402

Lin, Z., Sun, X., Chen, K., Strauss, H., Klemd, R., Smrzka, D., et al. (2022). Effects of sulfate reduction processes on the trace element geochemistry of sedimentary pyrite in modern seep environments. *Geochim. Cosmochim. Acta* 333, 75–94. doi: 10.1016/j.gca.2022.06.026

Liu, X., Fike, D., Li, A., Dong, J., Xu, F., Zhuang, G., et al. (2019). Pyrite sulfur isotopes constrained by sedimentation rates: Evidence from sediments on the East China Sea inner shelf since the late Pleistocene. *Chem. Geol.* 505, 66–75. doi: 10.1016/j.chemgeo.2018.12.014

Liu, X., Li, A., Fike, D. A., Dong, J., Xu, F., Zhuang, G., et al. (2020b). Environmental evolution of the East China Sea inner shelf and its constraints on pyrite sulfur contents and isotopes since the last deglaciation. *Mar. Geol.* 429, 106307. doi: 10.1016/j.margeo.2020.106307

Liu, J., Pellerin, A., Izon, G., Wang, J., Antler, G., Liang, J., et al. (2020a). The multiple sulphur isotope fingerprint of a sub-seafloor oxidative sulphur cycle driven by iron. *Earth Planet. Sci. Lett.* 536, 116165. doi: 10.1016/j.epsl.2020.116165

Lovley, D. R. (1991). Dissimilatory fe(III) and mn(IV) reduction. *Microbiol. Rev.* 55, 259–287. doi: 10.1128/mr.55.2.259–287.1991

Mao, S.-H., Zhang, H.-H., Zhuang, G.-C., Li, X.-J., Liu, Q., Zhou, Z., et al. (2022). Aerobic oxidation of methane significantly reduces global diffusive methane emissions from shallow marine waters. *Nat. Commun.* 13, 7309. doi: 10.1038/s41467–022-35082-y

McManus, J., Berelson, W. M., Klinkhammer, G. P., Hammond, D. E., and Holm, C. (2005). Authigenic uranium: Relationship to oxygen penetration depth and organic carbon rain. *Geochim. Cosmochim. Acta* 69, 95–108. doi: 10.1016/j.gca.2004.06.023

McManus, J., Berelson, W. M., Severmann, S., Poulson, R. L., Hammond, D. E., Klinkhammer, G. P., et al. (2006). Molybdenum and uranium geochemistry in continental margin sediments: Paleoproxy potential. *Geochim. Cosmochim. Acta* 70, 4643–4662. doi: 10.1016/j.gca.2006.06.1564

Miao, X., Liu, X., Li, Q., Li, A., Cai, F., Kong, F., et al. (2022). Porewater geochemistry indicates methane seepage in the Okinawa Trough and its implications for the carbon cycle of the subtropical West Pacific. *Palaeogeogr. Palaeoclimatol. Palaeoecol.* 607, 111266. doi: 10.1016/j.palaeo.2022.111266

Mogollón, J. M., Dale, A. W., Jensen, J. B., Schlüter, M., and Regnier, P. (2013). A method for the calculation of anaerobic oxidation of methane rates across regional scales: an example from the Belt Seas and The Sound (North Sea–Baltic Sea transition). *Geo-Mar. Lett.* 33, 299–310. doi: 10.1007/s00367–013-0329-z

Naehr, T. H., Eichhubl, P., Orphan, V. J., Hovland, M., Paull, C. K., Ussler, W., et al. (2007). Authigenic carbonate formation at hydrocarbon seeps in continental margin sediments: A comparative study. *Deep. Sea. Res. Part II. Top. Stud. Oceanogr.* 54, 1268–1291. doi: 10.1016/j.dsr2.2007.04.010

Naqvi, S. W. A., Bange, H. W., Farías, L., Monteiro, P. M. S., Scranton, M. I., and Zhang, J. (2010). Marine hypoxia/anoxia as a source of CH_4 and N_2O. *Biogeosciences* 7, 2159–2190. doi: 10.5194/bg-7–2159-2010

Nöthen, K., and Kasten, S. (2011). Reconstructing changes in seep activity by means of pore water and solid phase Sr/Ca and Mg/Ca ratios in pockmark sediments of the Northern Congo Fan. *Mar. Geol.* 287, 1–13. doi: 10.1016/j.margeo.2011.06.008

Peketi, A., Mazumdar, A., Joao, H. M., Patil, D. J., Usapkar, A., and Dewangan, P. (2015). Coupled C–S–Fe geochemistry in a rapidly accumulating marine sedimentary system: Diagenetic and depositional implications. *Geochem. Geophys. Geosyst.* 16, 2865–2883. doi: 10.1002/2015gc005754

Peketi, A., Mazumdar, A., Joshi, R. K., Patil, D. J., Srinivas, P. L., and Dayal, A. M. (2012). Tracing the paleo sulfate-methane transition zones and H2S seepage events in marine sediments: An application of c-S-Mo systematics. *Geochem. Geophys. Geosyst.* 13 (10). doi: 10.1029/2012gc004288

Qiu, J., Liu, J., Yue, N., Wang, S., and Mai, D. D. (2018). Distribution and characteristics of hazardous geological features in the marine coastal and offshore areas of Zhejiang Province, East China sea. *J. Ocean. Univ. China* 17, 1318–1324. doi: 10.1007/s11802–018-3671-y

Reeburgh, W. S. (2007). Oceanic methane biogeochemistry. *Chem. Rev.* 107, 486–513. doi: 10.1021/cr050362v

Regnier, P., Dale, A. W., Arndt, S., LaRowe, D. E., Mogollón, J., and Van Cappellen, P. (2011). Quantitative analysis of anaerobic oxidation of methane (AOM) in marine sediments: A modeling perspective. *Earth-Sci. Rev.* 106, 105–130. doi: 10.1016/j.earscirev.2011.01.002

Rhee, T. S., Kettle, A. J., and Andreae, M. O. (2009). Methane and nitrous oxide emissions from the ocean: A reassessment using basin-wide observations in the Atlantic. *J. Geophys. Res. Atmospheres.* 114, D12304. doi: 10.1029/2008jd011662

Rice, D. D., and Claypool, G. E. (1981). Generation, accumulation, and resource potential of biogenic gas. *AAPG. Bull.* 65, 5–25.

Robbins, J. A., and Edgington, D. N. (1975). Determination of recent sedimentation rates in Lake Michigan using Pb-210 and Cs-137. *Geochim. Cosmochim. Acta* 39.3, 285–304. doi: 10.1016/0016-7037(75)90198-2

Schoell, M. (1988). Multiple origins of methane in the Earth. *Chem. Geol.* 71, 1–10. doi: 10.1016/0009–2541(88)90101–5

Schoepfer, S. D., Shen, J., Wei, H., Tyson, R. V., Ingall, E., and Algeo, T. J. (2015). Total organic carbon, organic phosphorus, and biogenic barium fluxes as proxies for paleomarine productivity. *Earth-Sci. Rev.* 149, 23–52. doi: 10.1016/j.earscirev.2014.08.017

Schulz, H. D. (2006). "Quantification of early diagenesis: dissolved constituents in pore water and signals in the solid phase," in *Marine geochemistry* (Springer, Berlin, Heidelberg), 73–124. doi: 10.1007/3–540-32144–6_3

Sela-Adler, M., Herut, B., Bar-Or, I., Antler, G., Eliani-Russak, E., Levy, E., et al. (2015). Geochemical evidence for biogenic methane production and consumption in the shallow sediments of the SE Mediterranean shelf (Israel). *Cont. Shelf. Res.* 101, 117–124. doi: 10.1016/j.csr.2015.04.001

Shi, X., Liu, S., Qiao, S., Yang, Z., and Liu, Y. (2015). Geochemical characteristics, controlling factor and record of paleoclimate in sediments from eastern China seas. *Bull. Mineral. Petrol. Geochem.* 34, 885–894. doi: 10.3969/j.issn.1007-2802.2015.05.001

Sivan, O., Adler, M., Pearson, A., Gelman, F., Bar-Or, I., John, S. G., et al. (2011). Geochemical evidence for iron-mediated anaerobic oxidation of methane. *Limnol. Oceanogr.* 56, 1536–1544. doi: 10.4319/lo.2011.56.4.1536

Smrzka, D., Feng, D., Himmler, T., Zwicker, J., Hu, Y., Monien, P., et al. (2020). Trace elements in methane-seep carbonates: Potentials, limitations, and perspectives. *Earth-Sci. Rev.* 208, 103263. doi: 10.1016/j.earscirev.2020.103263

Song, L., Fan, D., Su, J., and Guo, X. (2023). Controls on shallow gas distribution, migration, and associated geohazards in the Yangtze subaqueous delta and the Hangzhou Bay. *Front. Mar. Sci.* 10. doi: 10.3389/fmars.2023.1107530

Sun, M.-S., Zhang, G.-L., Ma, X., Cao, X.-P., Mao, X.-Y., Li, J., et al. (2018). Dissolved methane in the East China Sea: Distribution, seasonal variation and emission. *Mar. Chem.* 202, 12–26. doi: 10.1016/j.marchem.2018.03.001

Tribovillard, N., Algeo, T. J., Lyons, T., and Riboulleau, A. (2006). Trace metals as paleoredox and paleoproductivity proxies: An update. *Chem. Geol.* 232, 12–32. doi: 10.1016/j.chemgeo.2006.02.012

Wang, X., Shi, X. F., Wang, G. Q., Qiao, S. Q., and Liu, T. (2013). Sedimentation rates and its indication to distribution of Yangtze sediment supply around the Yangtze (Changjiang) River Estuary and its adjacent area, China. *Earth Sci. J. China Univ. Geosci.* 38, 763–775. doi: 10.3799/dqkx.2013.074

Whiticar, M. J. (1999). Carbon and hydrogen isotope systematics of bacterial formation and oxidation of methane. *Chem. Geol.* 161, 291–314. doi: 10.1016/s0009–2541(99)00092–3

Whiticar, M. J., Faber, E., and Schoell, M. (1986). Biogenic methane formation in marine and freshwater environments: CO2 reduction *vs.* acetate fermentation—Isotope evidence. *Geochim. Cosmochim. Acta* 50, 693–709. doi: 10.1016/0016–7037(86)90346–7

Wu, Y., Fan, D., Wang, D., and Yin, P. (2020). Increasing hypoxia in the Changjiang Estuary during the last three decades deciphered from sedimentary redox-sensitive elements. *Mar. Geol.* 419, 106044. doi: 10.1016/j.margeo.2019.106044

Xie, D. F., Pan, C. H., Cao, Y., and Zhang, B. H. (2013). Decadal variations in the erosion/deposition pattern of the hangzhou bay and their mechanism in recent 50a. *Acta Oceanol. Sin.* 35, 121–128. doi: 10.3969/j.issn.0253-4193.2013.04.015

Xie, D., Pan, C., Wu, X., Gao, S., and Wang, Z. B. (2017). Local human activities overwhelm decreased sediment supply from the Changjiang River: Continued rapid accumulation in the Hangzhou Bay-Qiantang Estuary system. *Mar. Geol.* 392, 66–77. doi: 10.1016/j.margeo.2017.08.013

Xu, C., Wu, N., Sun, Z., Zhang, X., Geng, W., Cao, H., et al. (2018). Methane seepage inferred from pore water geochemistry in shallow sediments in the western slope of the Mid-Okinawa Trough. *Mar. Pet. Geol.* 98, 306–315. doi: 10.1016/j.marpetgeo.2018.08.021

Yang, T., Jiang, S., Ge, L., Yang, J., Wu, N., Zhang, G., et al. (2010). Geochemical characteristics of pore water in shallow sediments from Shenhu area of South China Sea and their significance for gas hydrate occurrence. *Chin. Sci. Bull.* 55, 752–760. doi: 10.1007/s11434–009-0312–2

Yang, J., Lai, X., and Chen, Z. (2021). Pockmarks and their genesis in Qingbang Island waters of eastern Zhoushan Archipelago. *J. Appl. Oceanogr.* 40, 251–259. doi: 10.3969/j.issn.2095-4972.2021.02.008

Yang, S., Li, C., Wang, Z., Wang, X., and Shu, J. (2013). Heterogeneity of geochemical compositions of the Changjiang River sediments and provenance indication. *Quat. Sci.* 33, 645–655. doi: 10.3969/j.issn.1001-7410.2013.04.03

Yang, S. L., Milliman, J. D., Li, P., and Xu, K. (2011). 50,000 dams later: Erosion of the Yangtze River and its delta. *Glob. Planet. Change* 75, 14–20. doi: 10.1016/j.gloplacha.2010.09.006

Ye, H., Yang, T., Zhu, G., Jiang, S., and Wu, L. (2016). Pore water geochemistry in shallow sediments from the northeastern continental slope of the South China sea. *Mar. Pet. Geol.* 75, 68–82. doi: 10.1016/j.marpetgeo.2016.03.010

Zhang, M., Chang, X., Hu, L., Bi, N., Wang, H., and Liu, X. (2021). Source-to-sink process of organic carbon on the inner shelf of the East China sea and its sedimentary records. *Acta Sedimentol. Sin.* 39, 593–609. doi: 10.14027/j.issn.1000–0550.2020.080

Zhang, M., Liu, X., Xu, F., Li, A., Gu, Y., Chang, X., et al. (2023). Organic carbon deposition on the inner shelf of the East China sea constrained by sea level and climatic changes since the last deglaciation. *J. Ocean. Univ. China* 22, 1300–1312. doi: 10.1007/s11802–023-5476-x

Zheng, Y., Zheng, H., Kissel, C., and Laj, C. (2011). Sedimentation rate control on diagenesis, East China Sea sediments. *Phys. Earth Planet. Inter.* 187, 301–309. doi: 10.1016/j.pepi.2011.05.005

Zopfi, J., Böttcher, M. E., and Jørgensen, B. B. (2008). Biogeochemistry of sulfur and iron in *Thioploca*-colonized surface sediments in the upwelling area off central Chile. *Geochim. Cosmochim. Acta* 72, 827–843. doi: 10.1016/j.gca.2007.11.031